Sun Effects in 2-D Aperture Synthesis Radiometry Imaging and Their Cancelation

Adriano Camps, *Senior Member, IEEE*, Mercé Vall-llossera, *Member, IEEE*, Núria Duffo, *Member, IEEE*, M. Zapata, Ignasi Corbella, *Member, IEEE*, Francesc Torres, and V. Barrena

***Abstract*—The Microwave Imaging Radiometer by Aperture Synthesis (MIRAS) is the single payload of the European Space Agency's (ESA) Soil Moisture and Ocean Salinity (SMOS) Earth Explorer Opportunity mission. MIRAS will be the first two-dimensional aperture synthesis radiometer for earth observation. Two-dimensional aperture synthesis radiometers can generate brightness temperature images by a Fourier synthesis process without mechanical antenna steering. To do so and have the necessary wide swath for earth observation, the array is formed by small and low directive antennas, which do not attenuate enough bright noise sources that may interfere with the measurements. This study analyzes the impact of the radio-frequency emission from the sun in the SMOS mission, reviews the basic image reconstruction algorithms, and proposes a technique to minimize sun effects.**

***Index Terms*—Antenna arrays, imaging, interferometry, radiometry.**

I. Introduction

THE MICROWAVE Imaging Radiometer by Aperture Synthesis (MIRAS) instrument [1], [2] is the single payload of the European Space Agency's (ESA) Soil Moisture and Ocean Salinity (SMOS) mission, and it will be the first two-dimensional (2-D) aperture synthesis radiometer for earth observation. The brightness temperature image reconstruction is performed through a Fourier synthesis process of the cross correlations $V_{12}^{p,q}$ measured between the bandpass signals $\mathrm{b}_1^p(t)$ and $\mathrm{b}_2^q(t)$, at p and q polarizations by every pair of elements in the array

$$\begin{aligned} V_{12}^{p,q} &\triangleq \frac{1}{\mathrm{k_B}\sqrt{\mathrm{B_1B_2}}\sqrt{\mathrm{G_1G_2}}}\cdot\frac{1}{2}\left\langle \mathrm{b}_1^p(t)\mathrm{b}_2^{q^*}(t)\right\rangle \\ &= \frac{1}{\sqrt{\Omega_1\Omega_2}}\iint\limits_{\xi^2+\eta^2\le 1}\frac{T_{\mathrm{B}}^{p,q}(\xi,\eta)-T_{\mathrm{rec}}}{\sqrt{1-\xi^2-\eta^2}} \\ &\quad\cdot F_{n1}^{p}(\xi,\eta)F_{n2}^{q^*}(\xi,\eta)\tilde{r}_{12}\left(-\frac{u_{12}\xi+v_{12}\eta}{f_0}\right) \\ &\quad\cdot\exp(-j2\pi(u_{12}\xi+v_{12}\eta))\,d\xi\,d\eta \end{aligned} \tag{1}$$

where $\mathrm{k_B}$ is the Boltzmann's constant, $\mathrm{B}_{1,2}$ and $\mathrm{G}_{1,2}$ are the receivers' noise bandwidth and power gain, $\Omega_{1,2}$ is the solid angle of the antennas, $T_{\mathrm{B}}(\xi,\eta)$ is the brightness temperature of the scene, T_{rec} is the physical temperature of the receivers [3], $F_{n1,2}^{p,q}(\xi,\eta)$ are the normalized antenna copolar voltage patterns at p and q polarizations, $\tilde{r}_{12}(-(u_{12}\xi+v_{12}\eta)/f_0)$ is the fringe-wash function, f_0 is the center frequency $(\lambda_0 = c/f_0)$, $(u_{12},v_{12}) = (x_2-x_1, y_2-y_1)/\lambda_0$ is the spatial frequency sampled (baseline) that depends on the antenna position difference, and the director cosines $(\xi,\eta) = (\sin\theta\cos\phi, \sin\theta\sin\phi)$ are defined with respect to the X and Y axes in the antenna reference frame [X is perpendicular to the orbital plane; Y is 32° upward titled from the velocity vector; see Fig. 1(a)].

In MIRAS the zero-baselines $T_{Am,m}^{p,q} \equiv V_{m,m}^{p,q}(0,0)$ are the elements of the Stokes vector measured by three redundant noise injection radiometers [(NIR) see Fig. 1(b)]

$$\begin{aligned} T_{Am,m}^{p,q} &\equiv V_{m,m}^{p,q}(0,0) \\ &= \frac{1}{\sqrt{\Omega_1\Omega_2}}\iint\limits_{\xi^2+\eta^2\le 1}\frac{T_{\mathrm{B}}^{p,q}(\xi,\eta)}{\sqrt{1-\xi^2-\eta^2}} \\ &\quad\cdot F_{n1}^{p}(\xi,\eta)F_{n2}^{q^*}(\xi,\eta)\,d\xi\,d\eta. \end{aligned} \tag{2}$$

In (2), if $p=q=X, T_{Am,m}^{XX}$ is the antenna temperature at X-polarization, if $p=q=Y, T_{Am,m}^{YY}$ antenna temperature at Y-polarization, and if $p=Y, q=X: T_A^{\mathrm{YX}} = (T_3+jT_4)/2$, where T_3 and T_4 are the third and fourth Stokes parameters in the antenna reference frame.

In the case of identical antenna patterns $(F_{n1,2}^{p,q}(\xi,\eta) \equiv F(\xi,\eta))$ and negligible fringe-washing effects $(\tilde{r}_{12}=1)$, (1) reduces to a Fourier transform

$$V(u,v) \overset{\mathcal{F}^{-1}}{\underset{\mathcal{F}}{\rightleftarrows}} \frac{1}{\sqrt{\Omega_1\Omega_2}}\frac{T_{\mathrm{B}}^{p,q}(\xi,\eta)-T_{\mathrm{rec}}}{\sqrt{1-\xi^2-\eta^2}}|F_n(\xi,\eta)|^2. \tag{3}$$

The array structure determines the antenna positions and the discrete samples of $V(u,v)$ that are measured, and (1) can be viewed as a Fourier series expansion. Additionally, if $T_{\mathrm{B}}^{p,q}(\xi,\eta)$ is viewed as a set of independent point sources, (1) can be discretized and (3) becomes a DFT. In MIRAS, the array is formed by three arms 120° apart, with 23 equally spaced antennas each [Fig. 1(b)]. The Y-array configuration leads to an hexagonal sampling of the (u,v) spatial frequency domain, which is optimum in terms of number of antennas and correlators [4]. To avoid aliasing in the unit circle in the image reconstruction process, the antennas must be spaced $1/\sqrt{3}$ wavelengths. However, to minimize the number of antennas for a given angular resolution in SMOS, the antenna spacing is 0.875 wavelengths, some aliasing exists, but a wide swath is preserved.

Manuscript received October 23, 2003; revised January 1, 2004. This work was supported in part by the Spanish Comisión Interministerial de Ciencia y Tecnología under Grant MCYT TIC2002-04 451-C02-01) and in part by EADS-CASA Space Division (Madrid, Spain), prime contractor of SMOS PLM during Phase B Activities.

A. Camps, M. Vall-llossera, N. Duffo, M. Zapata, I. Corbella, and F. Torres are with the Department of Signal Theory and Communications, Universitat Politècnica de Catalunya, E-08034 Barcelona, Spain.

V. Barrena is with the GMV SA, Tres Cantos, E-28760 Madrid, Spain.

Digital Object Identifier 10.1109/TGRS.2004.826561

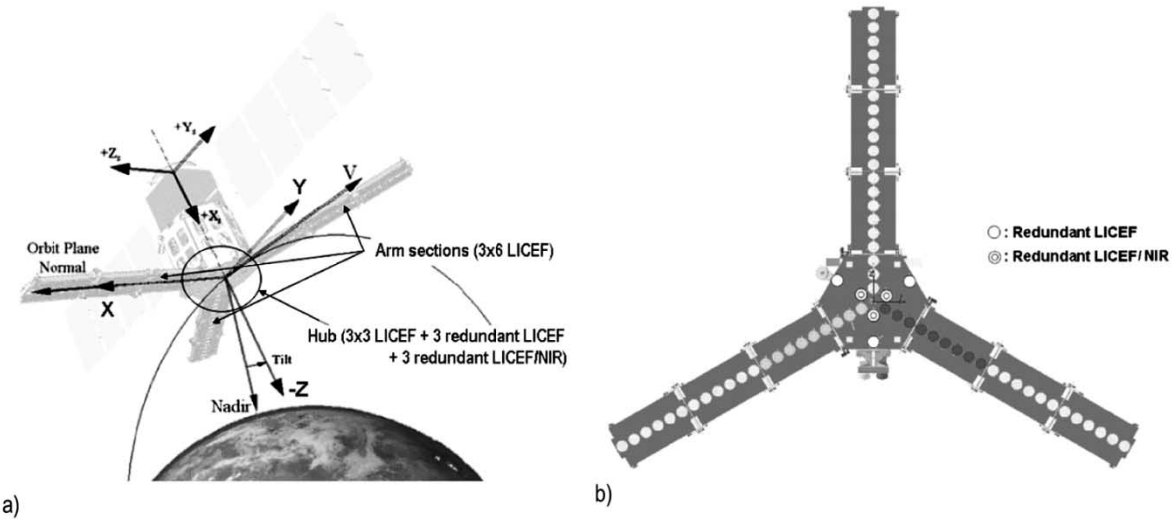

Fig. 1. (a) Instrument topology and observation geometry. Orbital parameters: mean altitude $=$ 755.5 km, eccentricity $=$ 0.001 165, inclination $=$ 98.416 470 773 546°, mean argument of perigee $=$ 90°, mean local time ascending node $=$ 6 h, mean anomaly $=$ −90°. (b) SMOS payload module phase B configuration (courtesy of EADS-CASA Espacio): three arms 120° apart, with 21 light and cost-effective front-end (LICEFs), plus two redundant LICEFs per arm (one LICEF and one LICEF/NIR) in its opposite direction in the hub. Antenna spacing is 0.875 wavelengths.

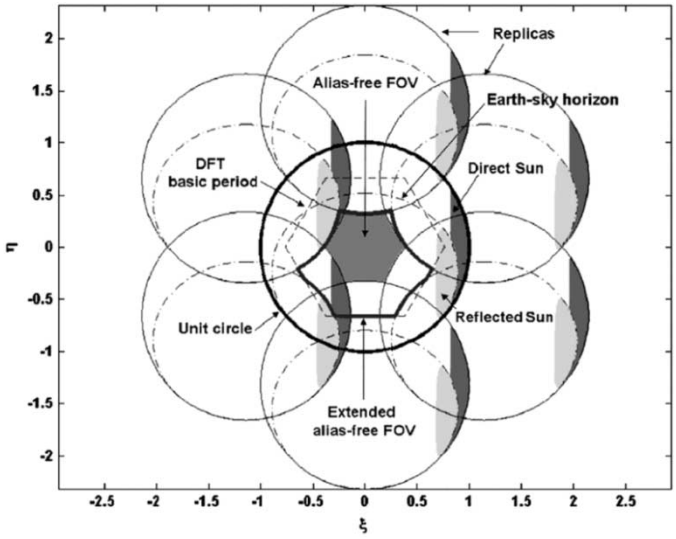

Fig. 2. Aliasing in 2-D aperture synthesis Y-shaped interferometric radiometers for an antenna spacing of 0.875 wavelengths, 32° array tilt, 30° array steering and 755 km platform height. Representation of the earth–sky horizon, unit circle, DFT basic period, geometric place of the sun positions (direct and reflected images), and their six closest replicas to the main DFT period. The extended alias-free FOV is the largest region where the brightness temperature images can be formed using the FOV extension presented in this work, as an extension of [7] to the case where sun and moon can be present.

II. Sun Effects

Fig. 2 shows the unit circle ($\xi^2 + \eta^2 = 1$) where the half-space in front of the array is mapped, and the closest six replicas (solid lines). The alias-free field of view is determined by the region in the unit circle limited by these six replicas. The earth–sky horizon is not circular, but has an ellipsoidal-like shape due to the 32° array tilting. For the SMOS orbital parameters [see caption for Fig. 1(a)] and the array tilting, the earth–sky horizon and the closest six replicas curves are shown in Fig. 2 as dashed–dotted lines. The hexagon (dashed line) is the basic period of the DFT, and brightness temperature replicas of this hexagonal "tile" are repeated periodically over the whole (ξ, η) plane. The region between the earth–sky horizon and the unit circle corresponds to the sky, which has a known brightness temperature much lower than that of the earth [5], [6]. As explained in Section III, this contribution can be subtracted from $V_{12}^{p,q}$ (1) to enlarge the alias-free field of view (AF-FOV) to the region limited by the six replicas of the earth–sky horizon (curved-hexagon solid line) [7]. However, in this process, any bright noise source or interference not properly canceled will degrade the radiometric performance of the instrument.

Fig. 3 shows also the geometric place of the positions occupied by the sun during a complete year for both direct (dark gray) and reflected (light gray) contributions. For the present SMOS configuration, a detailed analysis [8], [9] shows that the sun is present during approximately 96% of the time [Fig. 3(a) and (b)], and only $\sim$ 3% of the time it is eclipsed by the earth. The sun can be as high as 56.6° from the array boresight [Fig. 3(a) and (c)], while the reflected image can appear up to 44.7° from the array boresight. In addition, the brightness temperature of the sun depends on the solar cycle and can have strong fluctuations. Therefore, it is not obvious how to model and compensate sun effects. In Section IV, a method to deal with this problem is presented.

III. Review of Image Reconstruction Algorithms

The image reconstruction algorithm described in [7] allows to extend the AF-FOV up to the earth replicas (Fig. 2) by subtracting to the visibility samples the contributions from the following:

- the physical temperature of the receivers (T_{rec}): $V_R^{p,q}(u,v)$, which appear as offsets in the visibility samples, except at the zero baseline, $\bar{T}_A^{p,q} = V_R^{p,q}(0,0) = \sum_{\forall m} T_{Am,m}^{p,q}/3$, which is computed as the average of the three NIR measurements (2);
- the sky: $V_{\mathrm{sky}}(u,v)$;
- a constant brightness temperature in the region occupied by the earth: $V_{\mathrm{earth}}^{p,q}(u,v) = T_{\mathrm{earth}}^{p,q}\bar{V}_{\mathrm{earth}}^{p,q}(u,v)$, whose

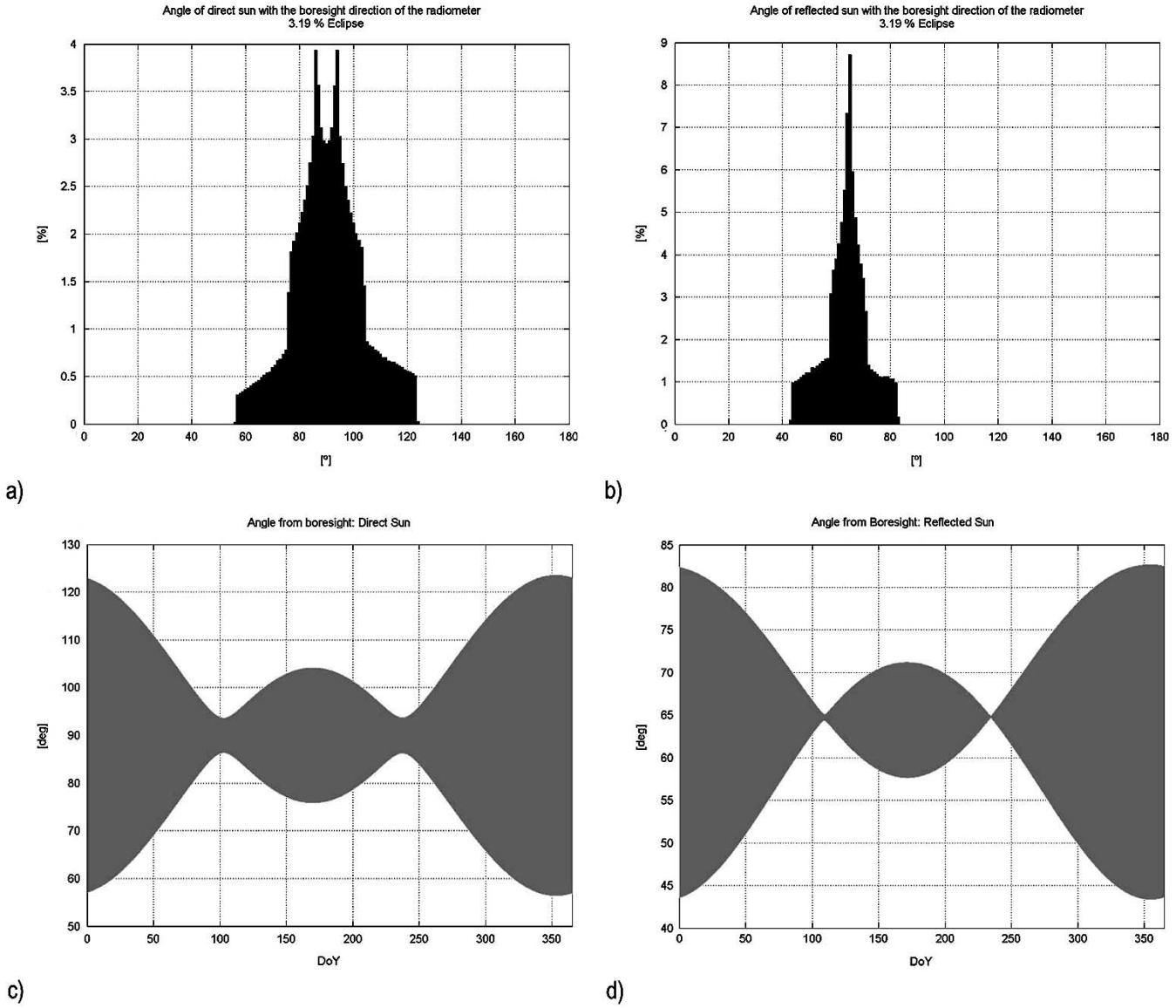

Fig. 3. (a) Histogram (1° bins) of the angle of direct sun directions with respect to the array boresight as a function of the day of the year. Angle $>90°$ means days when the sun is behind the array during part of the day. (b) Histogram (1° bins) of the angle of reflected sun directions with respect to the array boresight as a function of the day of the year. (c) Angle of direct sun directions with respect to the array boresight as a function of the day of the year. Angle $>90°$ means days when the sun is behind the array during part of the day. (d) Angle of reflected sun directions with respect to the array boresight as a function of the day of the year.

amplitude ($T^{p,q}_{\text{earth}}$) is determined so that the differential visibility ($\Delta V(u,v)$) at the origin is zero

$$\Delta V^{p,q}(u,v) = V^{p,q}(u,v) - V^{p,q}_R(u,v) - V^{p,q}_{\text{sky}}(u,v) - T^{p,q}_{\text{earth}}\bar{V}_{\text{earth}}(u,v) \tag{4}$$

$$V^{p,q}_R \triangleq \frac{1}{\sqrt{\Omega_1\Omega_2}} \iint\limits_{\xi^2+\eta^2\le 1} \frac{-T_{\text{rec}}}{\sqrt{1-\xi^2-\eta^2}} \cdot \hat{F}^{p}_{n1}(\xi,\eta)\hat{F}^{q^*}_{n2}(\xi,\eta)\hat{\hat{r}}_{12}\left(-\frac{u_{12}\xi+v_{12}\eta}{f_0}\right) \cdot \exp(-j2\pi(u_{12}\xi+v_{12}\eta))\,d\xi\,d\eta \tag{5}$$

$$V^{p,q}_{\text{sky}} \triangleq \frac{1}{\sqrt{\Omega_1\Omega_2}} \iint\limits_{\xi^2+\eta^2\subset\text{sky}} \frac{T^{p,q}_{\text{B sky}}(\xi,\eta)}{\sqrt{1-\xi^2-\eta^2}} \cdot \hat{F}^{p}_{n1}(\xi,\eta)\hat{F}^{q^*}_{n2}(\xi,\eta)\hat{\hat{r}}_{12}\left(-\frac{u_{12}\xi+v_{12}\eta}{f_0}\right) \cdot \exp(-j2\pi(u_{12}\xi+v_{12}\eta))\,d\xi\,d\eta \tag{6}$$

$$\bar{V}^{p,q}_{\text{earth}} \triangleq \frac{1}{\sqrt{\Omega_1\Omega_2}} \iint\limits_{\xi^2+\eta^2\subset\text{earth}} \frac{1}{\sqrt{1-\xi^2-\eta^2}} \cdot \hat{F}^{p}_{n1}(\xi,\eta)\hat{F}^{q^*}_{n2}(\xi,\eta)\hat{\hat{r}}_{12}\left(-\frac{u_{12}\xi+v_{12}\eta}{f_0}\right) \cdot \exp(-j2\pi(u_{12}\xi+v_{12}\eta))\,d\xi\,d\eta \tag{7}$$

where

$$T^{p,q}_{\text{earth}} = \frac{\bar{T}^{p,q}_A - V^{p,q}_{\text{sky}}(0,0)}{\bar{V}^{p,q}_{\text{earth}}(0,0)} \tag{8}$$

and the symbol "^" refers to measured antenna patterns and fringe-wash functions that may be slightly different with respect to the actual ones. As compared to the original formulation [7], the term $V^{p,q}_R$ in (4) has been included in baselines different from $(u,v) = (0,0)$ to account for the new T_{rec} term in the visibility function (1). The term $V^{p,q}_{\text{sky}}$ has been modified from

the original formulation to account for sky and galactic background radiation inhomogeneities. Equation (1) reduces now to

$$\Delta V^{p,q} \triangleq \frac{1}{\sqrt{\Omega_1\Omega_2}} \iint\limits_{\xi^2+\eta^2\subset\text{earth}} \frac{\Delta T_{\text{B}}^{p,q}(\xi,\eta)}{\sqrt{1-\xi^2-\eta^2}} \cdot \hat{F}_{n1}^{p}(\xi,\eta)\hat{F}_{n2}^{q^*}(\xi,\eta)\hat{\tilde{r}}_{12}\left(-\frac{u_{12}\xi+v_{12}\eta}{f_0}\right) \cdot \exp(-j2\pi(u_{12}\xi+v_{12}\eta))\,d\xi\,d\eta \tag{9}$$

which can be solved for $\Delta T_{\text{B}}^{p,q}(\xi,\eta)\hat{=}T_{\text{B}}^{p,q}(\xi,\eta)-T_{\text{earth}}^{p,q}$, i.e., the deviations of the brightness temperature over the mean value $T_{\text{earth}}^{p,q}$ in the AF-FOV. The solution of (9) can be reached by discretizing all the visibility samples for all (ξ,η) points and then solving the set of linear equations of the form $\overline{\Delta V^{p,q}} = \bar{\bar{G}}\overline{\Delta T_B^{p,q}}$ using the following:

- an iterative algorithm as described in [7];
- the pseudoinverse matrix as in [10] in the one-dimensional case; or
- a conjugate-gradient algorithm as in [11] in the 2-D case.

Note that in (9) the measured antenna patterns and fringe-wash functions are the estimated ones used in the image reconstruction.

IV. Including Sun and Moon Effects in 2-D Aperture Synthesis Interferometric Radiometer Image Reconstruction Algorithms

Before including the effect of the sun and moon in (4), the following considerations must be taken into account.

- Direct sun images appear in the AF-FOV through replicas of the main DFT period.
- Reflected sun and moon images appear overlapped with earth replicas (Fig. 2) and, therefore, is more difficult for the image reconstruction algorithm to take them into account properly.
- Positions of the direct and reflected sun and moon are known *a priori*, since they depend on the relative position and orientation between the sun or moon and the platform, as well as its attitude.
- Shape of the direct sun and moon images is not perturbed, while the reflected ones can be distorted by the scattering.
- Sun and moon contribute to $\bar{T}_A^{p,q}$ and, therefore, affect the average brightness temperature of the earth [$T_{\text{earth}}^{p,q}$ in (8)], which translates into an image bias.
- At L-band, the brightness temperature of the sun presents strong fluctuations. A procedure is needed to estimate it from the data itself, or it can be measured by radio-telescope observations. The brightness temperature of the moon is rather constant, about 250 K [12].

At this point, the brightness temperature of the sun can be first estimated from the data itself, as explained below. Since the sun and moon are seen under an angle[1] much smaller than the angular resolution of the instrument,[2] they appear as point sources. The visibility samples (without units) that would be measured by the instrument corresponding to unitary point sources located at the positions of the direct or reflected sun and moon $(1\cdot\delta(\xi-\xi_{\text{sun/moon,dir/ref}},\eta-\eta_{\text{sun/moon,dir/ref}}))$ can be computed as

$$\bar{V}_{\text{sun/moon,dir/ref}}^{p,q} = \frac{1}{\sqrt{\Omega_1\Omega_2}} \cdot \iint\limits_{\xi^2+\eta^2\le 1} \frac{\delta(\xi-\xi_{\text{sun/moon,dir/ref}},\eta-\eta_{\text{sun/moon,dir/ref}})}{\sqrt{1-\xi^2-\eta^2}} \cdot \hat{F}_{n1}^{p}(\xi,\eta)\hat{F}_{n2}^{q^*}(\xi,\eta)\hat{\tilde{r}}_{12}\left(-\frac{u_{12}\xi+v_{12}\eta}{f_0}\right) \cdot \exp(-j2\pi(u_{12}\xi+v_{12}\eta))\,d\xi\,d\eta \tag{10}$$

where $\xi_{\text{sun/moon,dir/ref}}$ and $\eta_{\text{sun/moon,dir/ref}}$ can be determined by geometrical relationships or from the data itself looking to the peak's position in (12).

- A "raw" brightness temperature image is formed by taking the inverse Fourier transform of

$$\hat{T}_B^{p,q} = F^{-1}\left[V^{p,q}(u,v) - V_R^{p,q}(u,v)\right]. \tag{11}$$

- The normalized direct and reflected sun and moon images (without units) are estimated from

$$\hat{\tilde{T}}_{\text{sun/moon,dir/ref}}^{p,q} = F^{-1}\left[\bar{V}_{\text{sun/moon,dir/ref}}^{p,q}(u,v)\right] \tag{12}$$

  if the direct and/or reflected sun and/or moon are visible.
- A first estimate of the sun brightness temperature is obtained as the ratio of $\hat{T}_B^{p,q}(\xi_{\text{sun,dir}},\eta_{\text{sun,dir}})$ (units Kelvin) and $\hat{\tilde{T}}_{\text{sun,dir}}^{p,q}(\xi_{\text{sun,dir}},\eta_{\text{sun,dir}})$ (without units) in the direction of the direct sun

$$T_{\text{sun,dir}}^{p,q} = \hat{T}_B^{p,q}(\xi_{\text{sun,dir}},\eta_{\text{sun,dir}}) \Big/ \hat{\tilde{T}}_{\text{sun/dir}}^{p,q}\,(\xi_{\text{sun,dir}},\eta_{\text{sun,dir}}). \tag{13}$$

- The same ratio is computed at the direction of the reflected sun

$$T_{\text{sun,ref}}^{p,q} = \hat{T}_B^{p,q}(\xi_{\text{sun,ref}},\eta_{\text{sun,ref}}) \Big/ \hat{\tilde{T}}_{\text{sun,ref}}^{p,q}\,(\xi_{\text{sun,ref}},\eta_{\text{sun,ref}}). \tag{14}$$

- Since the image of the direct sun appears overlapped with the image of the earth, an estimate of the power reflection coefficient at $(\xi_{\text{sun,ref}},\eta_{\text{sun,ref}})$ is performed as the ratio of (14) and (13)

$$\hat{\Gamma}^{p,q} = T_{\text{sun,ref}}^{p,q} \Big/ T_{\text{sun,dir}}^{p,q}. \tag{15}$$

- A better estimate of $T_{\text{sun,dir}}^{p,q}$ is computed by subtracting to (13) an estimated contribution from the earth's background and the scattered down-welling (atmosphere + sky) radiation

$$T_{\text{sun,dir}}^{p,q'} = T_{\text{sun,dir}}^{p,q} - (1-\Gamma^{p,q})T_{\text{ph}} - \Gamma^{p,q}T_{\text{SC}} \approx T_{\text{sun,dir}}^{p,q} - (1-\Gamma^{p,q})T_{\text{ph}} \tag{16}$$

  where the physical temperature is approximated by $T_{\text{ph}} \approx 290$ K.

[1]The sun and moon disks seen from the earth are $\sim 0.5^\circ$ wide, although the solar disk can appear larger at L-band.

[2]The angular resolution of MIRAS ranges from 1.60° to 2.25°, if the rectangular or Blackman windows are used to taper the visibility samples, respectively.

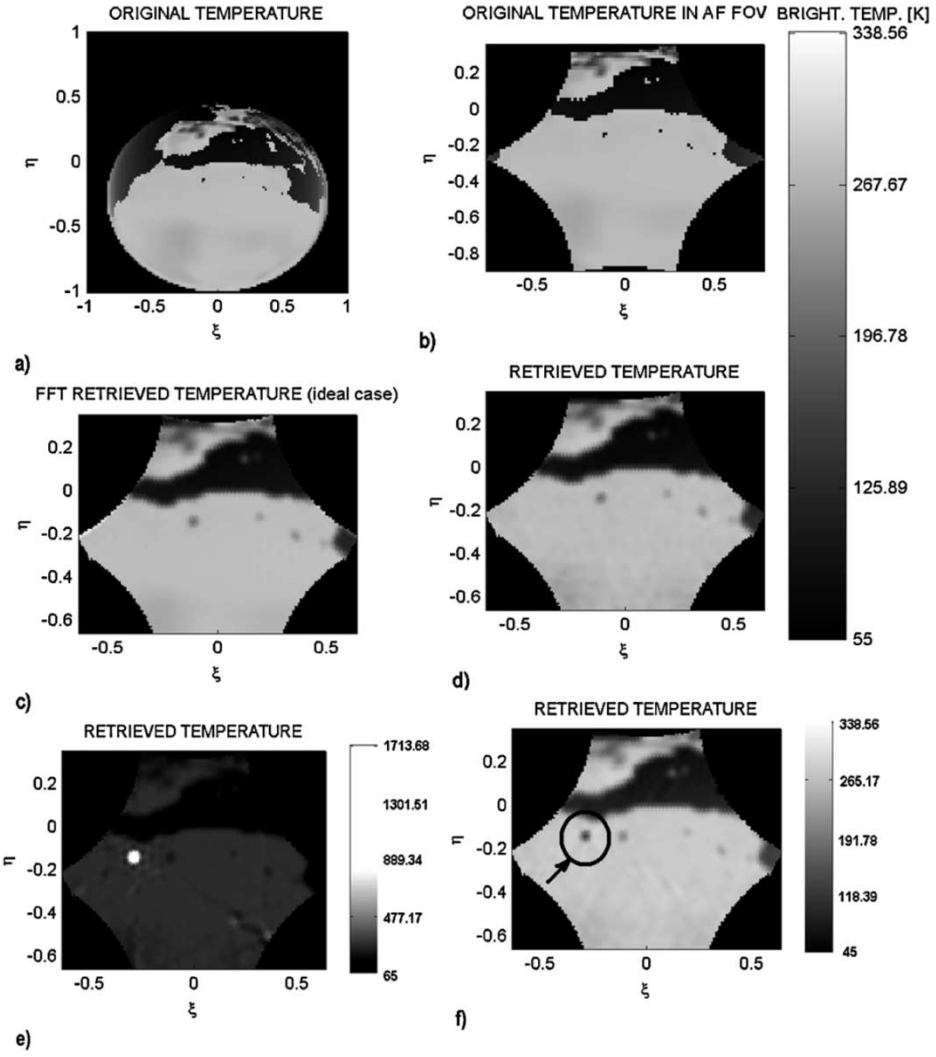

Fig. 4. SEPS simulation results (Y-polarization) corresponding to a pass over the Western Mediterranean region (Spain and North of Africa). (a) SEPS input brightness temperature distribution. (b) Original brightness temperature in the unit circle limited by replicas of earth–sky horizons. (c) Ideal FFT-reconstructed brightness temperature in the extended AF-FOV. (d) Reconstructed brightness temperature in the extended AF-FOV without sun/moon effects. (e) Same as (d), but with sun effects: the alias image of direct sun appears as a bright spot in the image. (f) After sun cancelation the image looks like (d).

In the case of the moon, since the instrument's angular resolution is 2.25° and $T_{\mathrm{moon,dir}} \approx 250$ K [10], the amplitude of the moon's image is approximately $(0.5^\circ/2.25^\circ)^2 250\ \mathrm{K} \approx 12$ K, which is easily masked by the variations of the brightness temperature of the earth's background, and the procedure described above does not perform satisfactorily. Therefore, an estimate of the moon's brightness temperature is needed [10].

Once the amplitude of the four different contributions are properly estimated, the corresponding visibility samples can be computed from (10)

$$V^{p,q}_{\mathrm{sun/moon,dir/ref}}(u,v) = T^{p,q}_{\mathrm{sun/moon,dir/ref}} \cdot \bar{V}^{p,q}_{\mathrm{sun/moon,dir/ref}}(u,v) \quad (17)$$

and then included in (4)

$$\begin{aligned}\Delta V^{p,q}(u,v) =& V^{p,q}(u,v) - V^{p,q}_R(u,v) - V^{p,q}_{\mathrm{sky}}(u,v) \\ & - T^{p,q}_{\mathrm{earth}} \bar{V}_{\mathrm{earth}}(u,v), -T'_{\mathrm{sun,dir}} \bar{V}^{p,q}_{\mathrm{sun,dir}}(u,v) \\ & - T_{\mathrm{sun,ref}} \bar{V}^{p,q}_{\mathrm{sun,ref}}(u,v) \\ & - T_{\mathrm{moon,dir}} \bar{V}^{p,q}_{\mathrm{moon,dir}}(u,v) \\ & - T_{\mathrm{moon,ref}} \bar{V}^{p,q}_{\mathrm{moon,ref}}(u,v) \end{aligned} \quad (18)$$

from where $T^{p,q}_{\mathrm{earth}}$ can be computed as in (19), shown at the bottom of the page. Now, (9) with sun and moon effects removed can be solved by any of the image reconstruction methods discussed [7], [10], [11].

$$T^{p,q}_{\mathrm{earth}} = \frac{\bar{T}^{p,q}_A - V^{p,q}_{\mathrm{sky}}(0,0) - T'_{\mathrm{sun,dir}} \bar{V}^{p,q}_{\mathrm{sun,dir}}(u,v) - T_{\mathrm{sun,ref}} \bar{V}^{p,q}_{\mathrm{sun,ref}}(0,0) - T_{\mathrm{moon,dir}} \bar{V}^{p,q}_{\mathrm{moon,dir}}(0,0) - T_{\mathrm{moon,ref}} \bar{V}^{p,q}_{\mathrm{moon,ref}}(0,0)}{\bar{V}^{p,q}_{\mathrm{earth}}(0,0)} \quad (19)$$

TABLE I
RADIOMETRIC ERRORS UNDER DIFFERENT CONDITIONS: BIAS IN THE EXTENDED AF-FOV AND RMS ERROR IN A CIRCLE CENTERED AT $(0, -0.24)$ OF RADIUS 0.3

Image radiometric error: bias and rms	$T_{y\,bias}$	$T_{x\,bias}$	σ_{Ty}	σ_{Tx}
Sun and Moon off	5.55 K	1.01 K	2.13 K	2.14 K
Sun and Moon on: without cancellation algorithm	5.67 K	2.23 K	14.15 K	15.62 K
Sun and Moon on: with cancellation algorithm	4.40 K	0.81 K	2.96 K	3.52 K

V. SIMULATION RESULTS

Fig. 4 shows simulation results perfomed using the SMOS end-to-end performance simulator (SEPS) [13] corresponding to a pass over the Western Mediterranean region (Spain and North of Africa):

- Fig. 4(a) shows the input brightness temperature distribution generated at Y-polarization using the internal database of geophysical parameters and the attitude and position of SMOS.
- Fig. 4(b) shows the original brightness temperature in the unit circle restricted to the region limited by replicas of earth–sky horizons, where theoretically the brightness temperature can be reconstructed.
- Fig. 4(c) shows the ideal FFT-reconstructed brightness temperature, without noise and instrumental errors, when the sun and moon are not activated in SEPS. Note that now the reconstruction is limited to the extended AF-FOV (Fig. 2), which is limited in the bottom part by the hexagonal DFT basic period. This image has the same angular resolution as the actual instrument, but does not have any errors. It is the reference image with respect to which the radiometric performance degradation is studied.

Three different scenarios have been considered when noise and instrumental errors are taken into account.Numerical results are presented in Table I:

1) Sun and moon not activated in SEPS. Fig. 4(d) shows the reconstructed brightness temperature in the extended AF-FOV. The brightness temperature bias are approximately 5.6 and 1.0 K at Y- and X-polarizations, respectively. This bias is dependent on the scene being imaged and it is due to the fact that the average brightness temperature in the region occupied by the earth is different from the average brightness temperature in the AF-FOV. This is a fundamental limitation of the instrument when operated in aliasing conditions, and will require some kind of vicarious calibration to compensate and track this bias. The root mean square (rms) errors are 2.13 and 2.14 K, at Y- and X-polarizations, which are very close to the theoretical predictions [8].
2) Sun and moon activated in SEPS, but no cancelation algorithm applied. Fig. 4(e) shows the reconstructed brightness temperature in the extended AF-FOV. The alias image of the direct sun image appears as a bright spot, and the tails of the impulse response extend all along the AF-FOV. For the impulse response of the reflected sun, in the aliased region, these tails enter in the AF-FOV and are also important. The global image biases vary less than $\sim$ 1.2 K (although this value is highly dependent on the sun position and the scenario), but the rms radiometric error dramatically increases up to 14–16 K, preventing from performing any soil moisture or ocean salinity retrievals. In other scenarios simulated, the rms radiometric error can increase even further, up to 80 K [8], [13] (see also http://www.tsc.upc.es/eef/reserach_lines/mrs/microcal/uCal02_Camps.pdf).
3) Sun and moon activated in SEPS, and cancelation algorithm applied. Fig. 4(f) shows the reconstructed brightness temperature in the extended AF-FOV. The image is no longer contaminated by a high bright spot from the sun. However, comparing Fig. 4(f) and (d), the brightness temperature in Fig. 4(f) (marked by a circle) is lower, which is due to the fact that the estimated sun brightness temperatures ($T^{yy'}_{\mathrm{sun,dir}} = 231\,949$ K and $T^{xx'}_{\mathrm{sun,dir}} = 234\,825$ K) are larger than the value used in the simulations (218 000 K). Despite this error, the impact of the sun is much smaller, with smaller bias, and rms radiometric errors of 2.96 and 3.52 K at Y- and X-polarizations. In addition, from an operational point of view, since on average, due to polarization mixing in the antenna reference frame, the estimated $T^{yy'}_{\mathrm{sun,dir}}$ and $T^{xx'}_{\mathrm{sun,dir}}$ values must be equal, and $T_{\mathrm{sun,dir}}$ has slow variations, the estimated values in a series of consecutive snapshots can be averaged so as to improve the estimation of $T_{\mathrm{sun,dir}}$ before applying the image reconstruction algorithm, or it can be directly measured from ground with a calibrated radio-telescope.

VI. CONCLUSION

This work has analyzed the effect of the presence of the sun in 2-D aperture synthesis radiometers for earth observation, and particularly in the SMOS mission of the European Space Agency. Due to aliasing in the Fourier synthesis imaging, replicas of the direct sun image appear overlapped with the image of the earth corrupting it, and making it useless for scientific purposes. This paper has reviewed a previous image reconstruction algorithm with a preprocessing technique to enlarge the alias-free FOV. The additional preprocessing necessary to account for the receivers' physical temperature term in the visibility function equation has been presented, as well as the procedure to estimate and cancel the effects of the presence of the sun and the moon. Simulation results using the SMOS end-to-end performance simulator show a significant improvement in the rms radiometric accuracy when the cancelation algorithm is applied, as compared to when it is not, even when the $T_{\mathrm{sun,dir}}$ estimates are based on a single snapshot. In an operational system, the algorithm performance can be improved by averaging estimates from consecutive snapshots.

ACKNOWLEDGMENT

The authors are very grateful to four anonymous reviewers whose comments have helped to increase the clarity of this paper.

REFERENCES

[1] M. Martín-Neira and J. M. Goutoule, "MIRAS—A two-dimensional aperture-synthesis radiometer for soil-moisture and ocean salinity observations," *ESA Bull.*, no. 92, pp. 95–104, Nov. 1997.

[2] P. Sivestrin, M. Berger, Y. Kerr, and J. Font, "ESA's second earth explorer opportunity mission: The Soil Moisture and Ocean Salinity Mission—SMOS," *IEEE Geosci. Remote Sensing Newslett.*, no. 118, pp. 11–14, Mar. 2001.

[3] I. Corbella, N. Duffo, M. Vall-llossera, A. Camps, and F. Torres, "The visibility function in interferometric aperture synthesis radiometry," *IEEE Trans. Geosci. Remote Sensing*, 2004, to be published.

[4] A. Camps, J. Bará, I. Corbella, and F. Torres, "The processing of hexagonally sampled signals with standard rectangular techniques: Application to 2D large aperture synthesis interferometric radiometers," *IEEE Trans. Geosci. Remote Sensing*, vol. 35, pp. 183–190, Jan. 1997.

[5] W. Reich, "A radio continuum survey of the northern sky at 1420 MHz," *Astron. Astrophys. Suppl. Series*, vol. 48, pp. 219–297, 1982.

[6] P. Reich and W. Reich, "A radio continuum survey of the northern sky at 1420 MHz. II," *Astron. Astrophys. Suppl. Series*, vol. 63, pp. 205–292, 1986.

[7] A. Camps, J. Bará, F. Torres, and I. Corbella, "Extension of the CLEAN technique to the microwave imaging of continuous thermal sources by means of aperture synthesis radiometers," *Progr. Electromagn. Res.*, vol. PIER 18, pp. 67–83, Jan. 1998.

[8] A. Camps, I. Corbella, F. Torres, M. Vall-llossera, and N. Duffo, "SMOS system performance model and error budget," Polytech. Univ. Catalonio, Barcelona, Spain, SO-TN-UPC-PLM-002 rev 3.20, Nov. 6, 2003.

[9] B. Duesmann, "SMOS sun and sun glint," ESTEC, Noordwijk, The Netherlands, EOP-PES System Analysis Office, SMOS Science Advisory Group Presentation, Oct. 1–2, 2003.

[10] C. S. Ruf, C. T. Swift, A. B. Tanner, and D. M. Levine, "Interferometric synthetic aperture microwave radiometry for the remote sensing of the earth," *IEEE Trans. Geosci. Remote Sensing*, vol. 26, pp. 597–611, Sept. 1988.

[11] R. Tomás, "Algoritmos de reconstrucción de imagen en radiometría por síntesis de apertura," School Telecommun, Eng., Polytech. Univ. Catalonia, Barcelona, Spain, Final Project Rep., 2002.

[12] Z. Kopal, *The Moon*, Dordrecht, Netherlands: Reidel, 1969.

[13] A. Camps, I. Corbella, M. Vall-llossera, N. Duffo, F. Marcos, F. Martínez-Fadrique, and M. Greiner, "The SMOS end-to-end performance simulator: Description and scientific applications," in *Proc. IGARSS*, Toulouse, France, July 21–25, 2003.

Adriano Camps (S'91–A'97–M'00–SM'02) was born in Barcelona, Spain, in 1969. He received the Telecommunications Engineering degree and the Ph.D. degree in telecommunications engineering in 1992 and 1996, respectively, both from the Polytechnic University of Catalonia (UPC), Barcelona, Spain.

From 1991 to 1992, he was with the ENS des Télécommunications de Bretagne, Bretagne, France, with an Erasmus Fellowship. In 1993, he joined the Electromagnetics and Photonics Engineering group, at the Department of Signal Theory and Communications, UPC, as an Assistant Professor, and since 1997 as an Associate Professor. In 1999, he was on sabbatical leave at the Microwave Remote Sensing Laboratory, University of Massachusetts, Amherst. His research interests are microwave remote sensing, with special emphasis in microwave radiometry by aperture synthesis techniques. He has performed numerous studies within the frame of European Space Agency SMOS Earth Explorer Mission. He is an Associate Editor of *Radio Science*.

Dr. Camps received the second national award of university studies in 1993, the INDRA award of the Spanish Association of Telecommunication Engineering to the best Ph.D. in 1997, the extraordinary Ph.D. award at the Universitat Politècnica de Catalunya in 1999, the First Duran Farell Award and the Ciudad de Barcelona Award, in 2000 and 2001, respectively, both for Technology Transfer; and in 2002, the Research Distinction of the Generalitat de Catalunya for contributions to microwave passive remote sensing. He was Chair of Cal '01. He is editor of the *IEEE Geoscience and Remote Sensing Newsletter* and President-Founder of the IEEE Geoscience and Remote Sensing Society Spain Chapter.

Mercè Vall-llossera (M'99) received the Senior Telecommunication Engineer and the Doctor Telecommunication Engineering degrees in 1990 and 1994, respectively, both from the Polytechnic University of Catalonia (UPC), Barcelona, Spain.

She has been lecturing and doing research at the Department of Signal Theory and Communications, UPC from 1990 until 1997 as an Assistant Professor and from 1997 until present as an Associate Professor. She spent a sabbatical year in Montreal with the scholarship of the "Programme Québécois de Bourses d'excellence" (1996–1997): "Stages de Formation postdoctorale au Québec pour jeunes diplômés étrangers." Her research interests include numerical methods in electromagnetism, microwave radiometry, antenna analysis, and design. Currently, her research is mainly related to the study of numerical methods applied to the sea surface emissivity and their characterization at L-band and the MIRAS/SMOS project.

Dr. Vall-llossera, along with the other member of the radiometry group at UPC, was awarded the "Primer Premio Duran Farell de Investigación Tecnológica" in 2002, and the "Primer Premio Ciutat de Barcelona d'Investigació Tecnològica" in 2001.

Núria Duffo (S'91–M'99) received the Telecommunication Engineer degree from the Polytechnic University of Catalonia (UPC), Barcelona, Spain, and the Doctor in Telecommunication Engineering from UPC, in 1990 and 1996, respectively.

Since 1997, she has been an Associate Professor at UPC. Her current research interests are numerical methods in electromagnetics, microwave radiometry, antenna analysis, and design.

M. Zapata, photograph and biography not available at the time of publication.

Ignasi Corbella (M'99) received the Telecommunications Engineering and Doctor Engineering degrees, both from Universitat Politècnica de Catalunya (UPC), Barcelona, Spain, in 1977 and 1983, respectively.

In 1976, he joined the School of Telecommunication Engineering in UPC as a Research Assistant in the Microwave Laboratory, were he worked on passive microwave integrated circuit design and characterization. During 1979, he worked at Thomson-CSF, Paris, France, on microwave oscillators design. In 1982, he became an Assistant Professor at UPC, an Associate Professor in 1986, and a Full Professor in 1993. He is currently teaching microwaves at the undergraduate level in UPC and has designed and taught graduate courses on nonlinear microwave circuits. During the school year 1998–1999, he worked at NOAA/Environmental Technology Laboratory, Boulder, CO, as a Guest Researcher, developing methods for radiometer calibration and data analysis. His research work in the Department of Signal Theory and Communications, UPC includes microwave airborne and satellite radiometry and microwave system design.

Francesc Torres received the Ingeniero and Doctor Ingeniero degrees in telecommunication engineering from the Polytechnic University of Catalonia (UPC), Barcelona, Spain, in 1988 and 1992, respectively

In 1988–1989, he was a Research Assistant in the RF System Division, European Space Agency, Noordwijk, The Netherlands, devoted to microwave device testing and characterization. In 1989, he joined the Antenna-Microwave-Radar group, UPC, where he is currently an Associate Professor. His main research interests are focused on the design and testing of microwave systems and subsystems. He is currently engaged in research on interferometric radiometers devoted to earth observation.

V. Barrena, photograph and biography not available at the time of publication.